A Monolithic Forward-View MEMS Laser Scanner With Decoupled Raster Scanning and Enlarged Scanning Angle for Micro LiDAR Applications

Dingkang Wang, Sanjeev J. Koppal, *Senior Member, IEEE*, and Huikai Xie, *Fellow, IEEE*

***Abstract*— This paper reports the design, fabrication, and characterization of a forward-view optical scanner realized by two vertical 2-axis MEMS mirrors integrated on a Silicon Optical Bench (SiOB). The mirror plate sizes of the first and second MEMS mirrors are 0.6×0.7 mm^2 and 1.2×1.4 mm^2, respectively. With the second MEMS mirror larger, the optical beam will not be truncated even during large-angle dynamic scanning. This dual-mirror configuration also enables multiple scanning modes, *e.g.*, an enlarged 2D field of view (FoV) by combining the scans of both mirrors, and a decoupled raster scanning by actuating the two mirrors separately. Experiments show that the enlarged 2D FoV reached 28°(h)×31°(v) and the FoV of the decoupled raster scanning reached 38°(h)×8°(v). The measured first resonances of the two mirrors were 2.09 kHz and 0.85 kHz, respectively. The overall size of the MEMS scanner was only $5.3\times5.8\times3.0$ mm^3, and its weight was 20 mg. This 2-axis forward optical scanner is much smaller and lighter than other two-mirror scanning modules, giving it a great potential for applications in miniature LiDAR for micro-robotics. [2020-0081]**

***Index Terms*— LiDAR, MEMS mirror, MEMS LiDAR, vertical MEMS mirror, electrothermal actuation, forward-view scanner.**

I. Introduction

IN RECENT years, light detection and ranging (LiDAR) modules have been widely explored and used in autonomous vehicles, including self-driving cars, automatic guided vehicles (AGVs) and unmanned aerial vehicles (UAVs) [1]. Autonomous vehicles can use LiDAR for obstacle detection and avoidance, object recognition and tracking, and simultaneous localization and mapping (SLAM) [2]–[4]. With the advancement of self-driving technologies, the demand for LiDAR is rapidly increasing. One of the crucial components for a LiDAR module is the optical scanner.

Motorized optical scanners have been widely applied in LiDAR, but they are bulky and consume high power [4]. Optical scanners based on MEMS mirrors, on the other hand, are small, power-efficient, and have wide 1D or 2D FoV, which can be used to build compact LiDAR systems [5]–[10]. For instance, Moss *et al.* reported a compact LiDAR system that utilized an electrostatic MEMS micromirror and had an overall size of 133 mm × 89 mm × 178 mm and a weight of about 2.27 kg [8]. Kasturi *et al.* demonstrated a UVA-borne LiDAR with an electrostatic MEMS mirror scanner that could fit into a small volume of 70 mm × 60 mm × 60 mm and weighted about only 50 g [9]. Kimoto *et al.* developed a small size 3D LiDAR prototype based on an electromagnetic resonant MEMS mirror and a motorized stage with a size of 87 mm × 118 mm × 85 mm for robotic vehicles [10]. All these cases, the optical scanners were side viewing. However for LiDAR on insect-like micro-robotics [11], compact forward-view two-axis optical scanners are needed [12].

One solution is to insert an additional regular mirror to fold the optical beam scanned by a two-axis MEMS mirror for forward-view scanning [13], [19]. For instance, Wang *et al.* developed a compact forward-viewing LiDAR prototype based on an electrothermal MEMS mirror and an additional fixed mirror to fold the laser beam, but the overall dimensions after packaged with the additional mirror were increased to 100 mm × 100 mm × 60 mm [19]. In addition to the assembling and packaging complication, this configuration runs into an issue of cross-coupling between the two scanning axes of the 2-axis MEMS mirror.

Another solution for forward-view optical scanning is to use two scanning MEMS mirrors to relay the optical beam for forward-view scanning [15]–[18]. When the two MEMS mirrors scan independently in two different axis, the coupling effect can be minimized. The overall dimensions of those scanning modules are reduced to 20-50 mm, but they are still one order of magnitude larger than single MEMS mirrors. In addition, to accommodate the room for the packaging, alignment, and assembly structures, the distance between the two mirrors cannot be very small, which will cause optical beam truncation, limit the scanning FoV, or require large mirror plates that in turn lower the scan speed and make the package size large.

In order to reduce the packaging size as well as the assembling and alignment efforts, we developed a method that successfully integrated two vertically-oriented electrothermal MEMS mirrors on a silicon optical bench (SiOB) by using bending bimorphs and stopper structures [19]. However, the two mirrors were identical, causing serious optical beam truncation. Also, only the second mirror scanned in two axes while the first mirror was not for scanning and was just

Manuscript received April 21, 2020; revised May 15, 2020; accepted June 9, 2020. This work was supported in part by the US Office of Naval Research under Award N00014-18-1-2663, and in part by the NSF Multi-functional Integrated System Technology (MIST) Center at the University of Florida. Subject Editor M. Rais-Zadeh. *(Corresponding author: Dingkang Wang.)*

Dingkang Wang and Sanjeev J. Koppal are with the Department of Electrical and Computer Engineering, University of Florida, Gainesville, FL 32611 USA (e-mail: noplaxochia@ufl.edu; sjkoppal@ece.ufl.edu).

Huikai Xie is with the School of Information and Electronics, Beijing Institute of Technology, Beijing 100081, China (e-mail: hk.xie@ieee.org).

Color versions of one or more of the figures in this article are available online at http://ieeexplore.ieee.org.

Digital Object Identifier 10.1109/JMEMS.2020.3001921

used to fold the optical beam because the second MEMS mirror could not capture and reflect the laser beams if the first mirror actively scanned. Thus, there existed a strong coupling between the two scanning axes as the structural design of the second mirror was symmetric in both axes. It could not generate a stable raster scanning pattern when one axis was actuated in the resonant mode while the other axis was actuated in the non-resonant mode.

In this paper, we report a new MEMS scanner that overcomes both coupling and beam truncation problems by making the two vertical mirrors with asymmetric actuation and different mirror sizes. The second mirror is larger than the first mirror, and both mirrors can be actuated in two axes. The two mirrors are integrated on one SiOB, which allows a short distance between the two mirrors as well as easy optical alignment. In the following, the dual vertical MEMS mirror design is first introduced. Then the MEMS fabrication process is described in detail. After that, the experimental results of the MEMS scanning characteristics are presented.

II. MEMS Design and Simulation

The new MEMS design is illustrated in Fig. 1(a), where both of the 2-axis MEMS mirrors (Mirror I and Mirror II) are standing upright from the silicon substrate and can scan independently. The two micromirrors are parallel to each other with a 45° angle to the incident optical beam. An alignment trench is designed on the SiOB substrate for easy placement and alignment of a pigtailed Graded Index (GRIN) lens. The mirror plate size of Mirror I is 0.6×0.7 mm^2, which allows a laser beam as large as 0.6 mm in diameter with an incident angle of 45°. The distance between the two mirror plates is only 0.9 mm, which is closer than any other assembled two-mirror scanners. The mirror plate of Mirror II is 1.2×1.4 mm^2. Thus, as shown in Fig. 1(c), the optical beam will not be truncated when Mirror I scans a maximum FoV of $\pm 10°$(h) $\times \pm 11°$(v). Both mirrors are electrothermally-actuated and based on the inverted-series-connected (ISC) bimorph actuation structure reported in [20].

The two bending bimorph arrays carry the electrical currents to the actuators from the bonding pads on the SiOB substrate separately, so the two mirrors can be actuated independently without any interference. Also note that both mirror plates are not square, resulting in a separation of the two tip-tilt modes of each mirror for the sake of decoupled scanning. These features can lead to several forward-view scanning modes, such as double quasi-static arbitrary pointing with enlarged FoV, decoupled quasi-static/resonant 2-axis raster scanning, and decoupled double resonant 2-axis Lissajous scanning.

The vertical orientation of the mirror frames is realized by using a bending bimorph-stopper mechanism similar to the one reported in [19]. The structure of the stopper is shown in Fig. 1(b). As shown in Fig. 1(b), the mirror frame is connected to an array of W/SiO_2 bimorphs. The bimorphs curl up due to the large difference between the thermal expansion coefficient of W and SiO_2. The radius of curvature of the bimorphs is determined by the deposition processes and thicknesses of the W and SiO_2 layers. By choosing a proper bimorph length, the end angle of the bimorphs can be exactly 90°. However, due to the unavoidable process variations, that

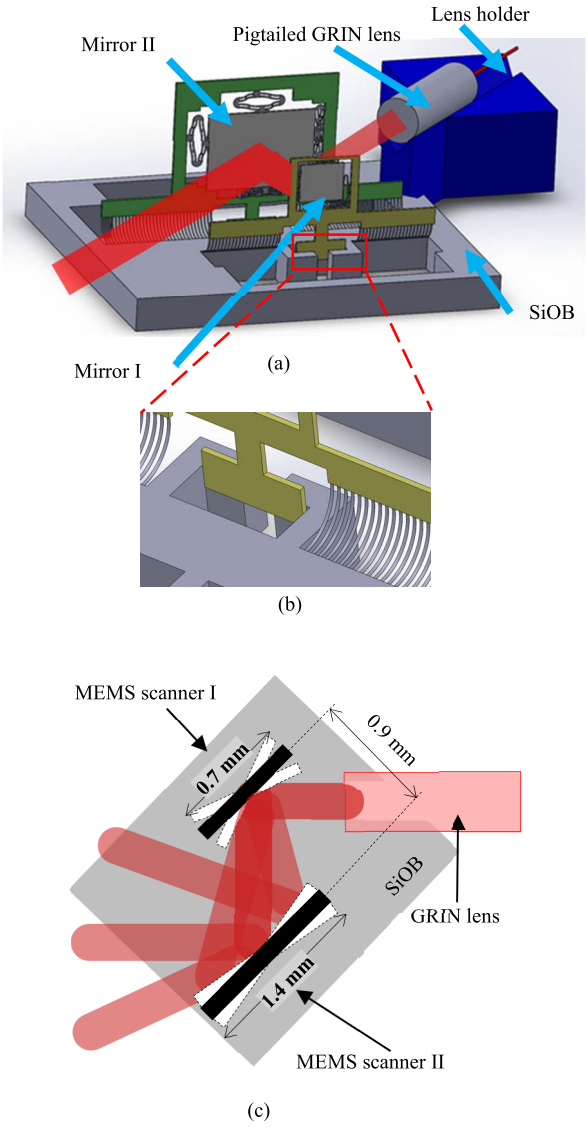

Fig. 1. (a) A 3D model of the MEMS scanner with two vertical mirrors on an SiOB with a pigtailed GRIN lens on a lens holder. (b) A zoom-in picture of the stopper structure of Mirror I. (c) This top-view picture shows the maximum scan FoV of the forward scanner.

90° orientation cannot be guaranteed. Thus, in order to ensure the vertical orientation of the mirror frame, the bending angle of the bimorphs is designed to be over 90°. At the same time, a stopper is designed to hold the extended bar of the mirror frame at the vertical direction. Again, due to the imperfection of microfabrication, the sidewalls of the stopper are typically not exactly vertical. Therefore, a fine-tuning deep-reactive-ion-etch (DRIE) silicon etching process is needed to minimize the vertical deviation, which will be further discussed in the next section.

COMSOL simulations are conducted to find the resonant modes of the device. The modal simulations are performed to both micromirrors. The two micromirrors have the same first four mode shapes, as shown in Fig. 2. The first four resonance frequencies of the two micromirrors are listed in Table I. The first mode has low resonance frequency, corresponding to the rotation mode of the frame of each micromirror. The second mode is the tilt mode. The tipping of the mirror plate is always coupled with the rotation of the frame as the bimorph beams

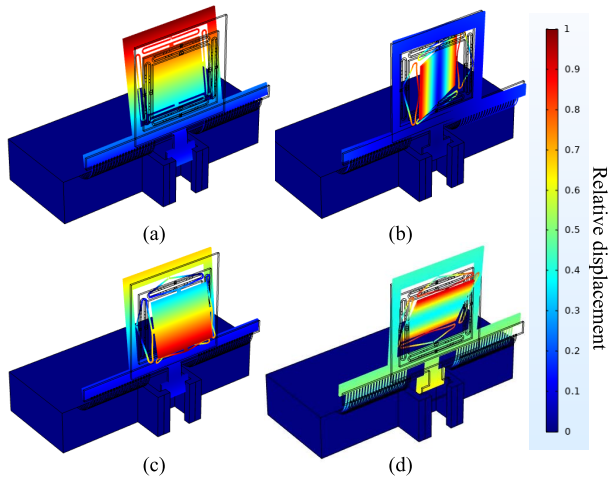

Fig. 2. The mode shapes of the first 4 modes of the two micromirrors. The mode shapes are (a) frame rotation mode, (b) tilt mode (mirror plate), (c) tip mode (mirror plate), (d) anti-tip mode (mirror plate).

TABLE I
THE RESONANT FREQUENCIES OF THE FIRST 4 MODES

Mode#	Mode description	Resonance frequency (kHz)	
		Mirror I	Mirror II
1	Frame rotation mode	0.38	0.27
2	Tilt mode (mirror plate)	2.16	0.90
3	Tip mode (mirror plate)	2.37	0.99
4	Anti-tip mode (mirror plate)	2.65	1.20

supporting the frame have relatively low stiffness along the tipping direction of the mirror plate. Thus the third and fourth modes are the tip and anti-tip modes of the mirror plate, respectively. Note that there is a separation between the tilt and tip resonant frequencies of either mirror. The purpose of this resonance separation is to reduce the cross-axis coupling as discussed in the Introduction.

III. DEVICE FABRICATION

The device is fabricated on an SOI (Silicon on insulator) wafer with a 40 μm-thick device layer, a 1 μm-thick buried oxide (BOX) layer and a 500 μm-thick handle layer. First, a 1 μm-thick PECVD (plasma-enhanced chemical vapor deposition) SiO_2 layer is deposited and patterned on the front side of the SOI wafer to form the bottom layer for the bimorphs containing SiO_2 as the bottom layer. Then a sputter and lift-off process of a Cr/Pt/Cr metal layer is performed to form the heaters for the bimorph actuators with a Pt thickness of 220 nm (Fig. 3(a)). Then the W with high tensile stress is sputtered and lift-off for the bending W/SiO_2 bimorph arrays (Fig. 3(b)). After that, a 0.1 μm PECVD SiO_2 layer is deposited and patterned using RIE, and then a 1-μm-thick Al layer is sputtered and patterned by a lift-off process to form the other layer of the bimorph actuators as well as the electrical wiring, pads and mirror surface coating (Fig. 3(c)). Another 1.1 μm PECVD SiO_2 layer is deposited and patterned by RIE dry etch to form bimorph actuators with SiO_2 as the top layer, and a thin layer of Al is patterned as the reflective mirror surface (Fig. 3(d)). A silicon carrier wafer is attached to the

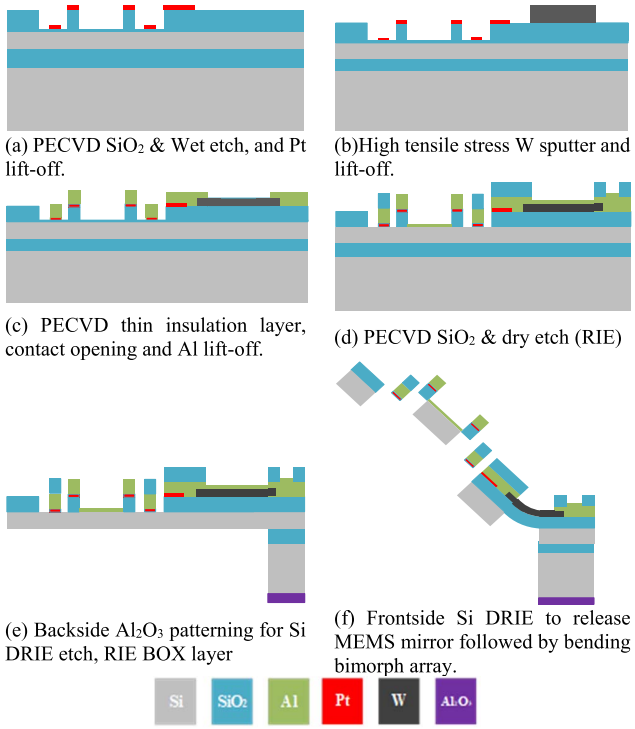

Fig. 3. Fabrication process flow.

front side of the SOI wafer for DRIE etch with a 150-nm sputtered Al_2O_3 as the mask. After etching a few testing samples for tuning the etching parameters, the DRIE recipe is set as 11 s etching plus 7 s passivation for each cycle. Once the BOX layer of the SOI wafer is exposed, the etching time of the DRIE cycles is increased to 14 s to fully remove polymer residues. The previouas recipe caused an undercut of 50 μm, while the undercut of the new recipe is only about 5 μm.

The DRIE etch stops at the BOX layer, and then the BOX layer is removed using HF vapor etching (Fig. 3(e)). After this step, the SOI wafer is separated from the carrier wafer. The release starts with an anisotropic DRIE that etches through the device layer to expose the sidewalls of the silicon underneath the bimorphs. Then an isotropic etching is done to undercut the silicon to release the bimorphs including both the bimorph actuators and the vertical bending bimorph arrays. Residual stresses in the thin films of the bimorphs result in initial out-of-plane displacements of the mirror plates (Fig. 3(f)).

Fig. 3(a) shows an SEM of a fabricated device, where the two vertically oriented micromirrors are each suspended by four ISC electrothermal Al/SiO_2 bimorph actuators, and the groove for the GRIN lens holder is 45° to the mirrors (Fig. 3(b)). More undercuts are seen on the silicon substrate because of the isotropic etch during the release process. The initial elevation of the mirror plate of Mirror I was about 120 μm and that of Mirror II was 150 μm. The aluminum mirror front surfaces are highly reflective to visible lights but lightly curved due to the stress between the aluminum layer and SOI mirror substrates. The backside of the mirror plates is also reflective and can be used to monitor the mirror scanning angles optically. The mirror frames popped up vertically to the substrate and their angles to the substrate were not exactly 90° but ranging from 85° to 95° for several released devices.

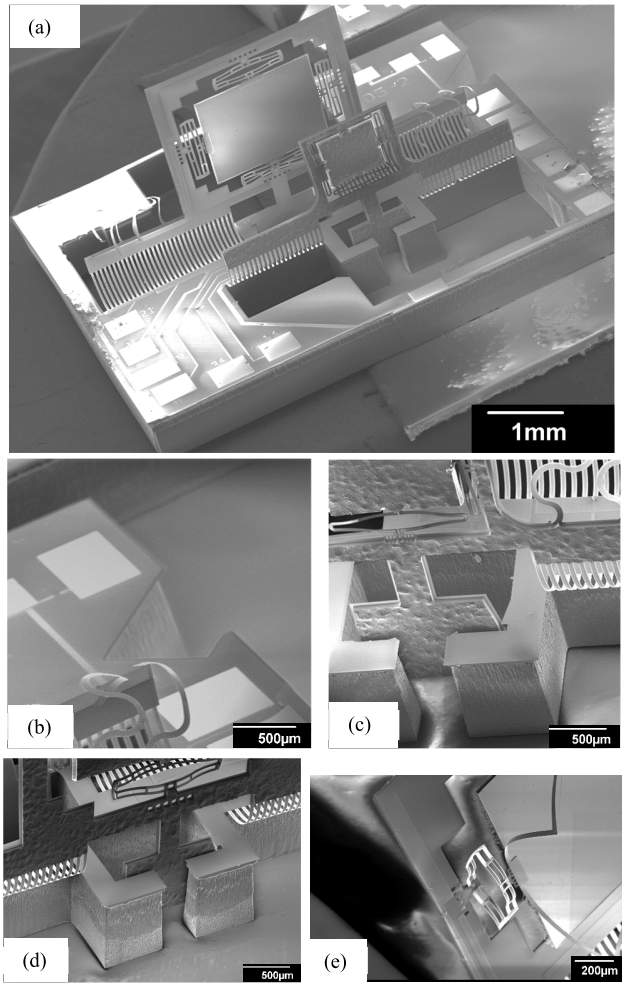

Fig. 4. (a) An SEM of the fabricated MEMS scanner. (b) The GRIN lens groove 45° to the Mirror I for laser beam alignment. (c) An SEM of the Mirror I stopper and an actuator. (d), (e) SEMs of the Mirror II stopper and actuators.

Details of the stopper and the actuators are shown in the SEMs in Figs. 4(b) to (e).

IV. Experiment Result

The measured quasi-static scanning angles of Mirror I and Mirror II are plotted in Figs. 5 (a) and (b), where their maximum optical scanning FoVs were 20°(h) × 22°(v) and 8°(h) × 9°(v), respectively. When both the Mirror I and Mirror II are actuated, the combined scanning FoV can be added up and achieve a wider scanning range. As shown in Fig. 6 (a), firstly, Mirror II was idle while the voltage applied to the left actuator of Mirror I was gradually increased from 0 to 3.5 V, leading to a maximum scanning angular range of +10° in the horizontal direction; then the left actuator of Mirror I was biased at 3.5 V while the voltage applied to the left actuator of Mirror II was increased from 0 to 4.5 V, leading to an enhanced optical scanning range of +14° in the horizontal direction. Repeating this procedure for the right actuators of the mirrors, a −14° scan range in the horizontal direction was also measured. In the vertical direction shown in Fig. 6 (b), those two angular ranges were +15.5° and −15.5°, respectively. Thus, the total combined FoV of the dual-mirror scanning reached 28°(h) × 31°(v).

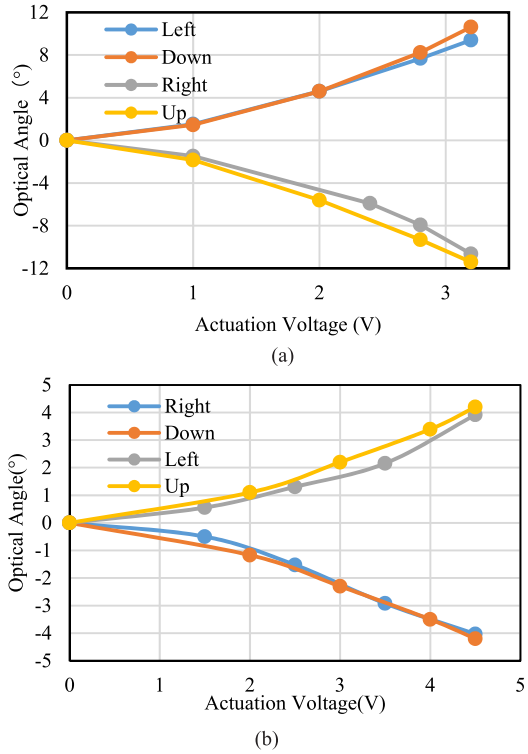

Fig. 5. The quasi-static responses of (a) Mirror I, (b) Mirror II.

TABLE II
Measured Resonant Frequencies of the First 4 Modes

Mode#	Mode description	Resonance frequency (kHz)	
		Mirror I	Mirror II
1	Frame rotation mode	0.41	0.29
2	Tilt mode (mirror plate)	2.09	0.85
3	Tip mode (mirror plate)	2.33	0.93
4	Anti-tip mode (mirror plate)	2.70	1.10

As shown in Fig. 6, the overall angular scan responses from combining the two mirrors were strongly nonlinear. This was due to the fact that both mirrors had noninear response when the actuating voltage of either mirror was in the range of 0-1 V. However, the response curves shown in Fig. 6 were obtained by simply actating one mirror while keeping the other static. This was only used to find out the maximum achievable angular scan ranges. In actual scanning applications, both micromirrors will be applied with in-phase driving signals with proper DC biases, so that the nonlinear portion can be avoided. As the two mirrors have different resonant frequencies and different thermal response, how to keep the two mirrors driven in phase is quite complex. More study is ongoing to figure out the phase sychronization.

The measured frequency responses of Mirror I and II are shown in Fig. 7, and the corresponding resonant frequencies of the first four modes are listed in Table II. It can be seen by comparing Table I and Table II that all the measurement agree well with the simulation values with discrepancies of 15% or less. This is mainly because of the uneven undercut of the mirror plates and mirror frames during the device

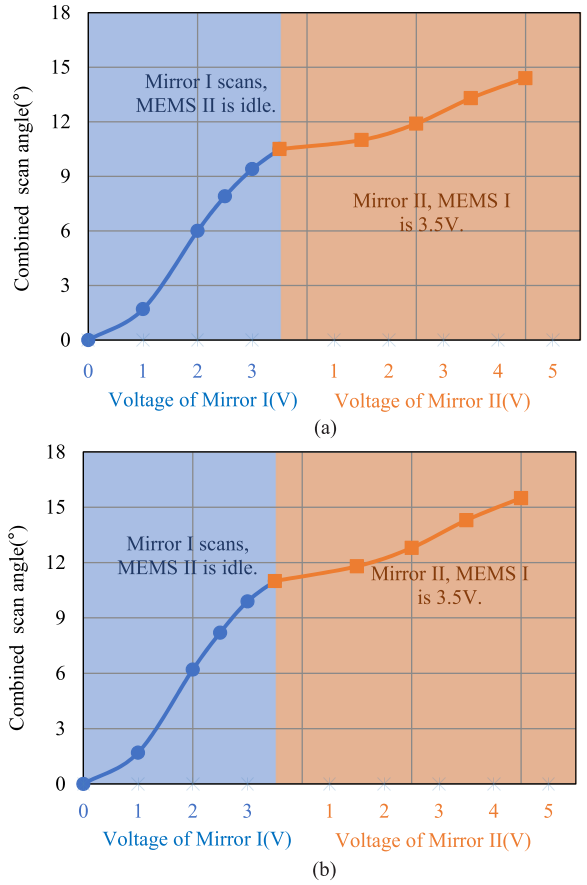

Fig. 6. The quasi-static responses of the combined scanning of both Mirror I and Mirror II in the (a) horizontal (b) vertical directions.

release fabrication step. The excitation of the first modes was due to the Joule heating generated by the currents passing through the conductive metal layers in the bending bimorph arrays. The low resonant frequency of the first modes may limit the overall working bandwidths. Fortunately, the frame rotation can be avoided by gluing the mirror frames with the stoppers. This frame rotation can also be used as an addtional scan at in the vertical direction if the mirror frames are not glued togethered with the stoppers. Also note that the two tip-tilt modes of either MEMS mirror were separated, which can reduce cross-axis coupling especially under resonant scanning. Furthermore, as can be seen in Fig. 7, the 3 dB bandwidths of these tip-tilt modes were about 30 Hz for Mirror I and about 20 Hz for Mirror II, corresponding to a Q factor of about 75 for Mirror I and 35 for Mirror II. The combination of the relative low Q and 20 dB/Dec thermal decay makes the type of electrothermal MEMS mirrors less sensitive to the enviromental changes especially under resonant scanning.

Fig. 8(a) shows the scan pattern when the vertical axis of Mirror I in the previous work [19] was driven to resonance while its horizontal axis was actuated at 20 Hz, where strong cross-axis coupling was observed. In order to minimize the coupling to obtain stable raster scanning patterns, Mirror I and Mirror II in this new design can be each driven at one axis and the scan axis of Mirror I is orthogonal to the scan axis of Mirror II. For example, as shown in Fig. 8(b), a stable high-line-density raster pattern was generated with

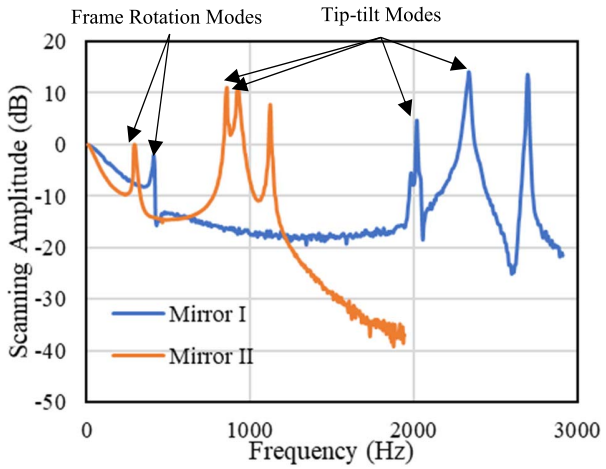

Fig. 7. The frequency responses of the two vertical mirrors.

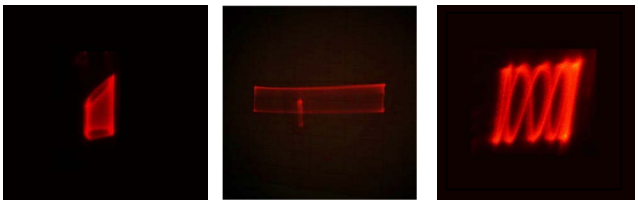

Fig. 8. Raster scan patterns: (a) driving Mirror I in the previous work [19] scanning vertically at resonance and horizontally at 20 Hz, the coupling effect can be noticed; (b) driving Mirror I vertically at resonance and Mirror II horizontally at 20 Hz, no coupling is noticed. (c) driving Mirror I vertically at 30 Hz, and Mirror II horizontally at 5 Hz, no coupling is noticed.

TABLE III
A COMPARISON OF 2-MIRROR DECOUPLED SCANNER MODULES

Dimensions (mm×mm×mm)	FoV	Ref.
75×49×28	30° ×30°	[15]
31×28×48	20° ×20°	[16]
~10×10×10	30.7° ×34.5°	[17]
25×30×24	20° ×20°	[18]
5.3×5.8×3.0	28° ×31°	This work

Mirror I actuated in the horizontal direction near the resonant frequency of 2.08 kHz, 36° and Mirror II actuated in the vertical direction at 20 Hz, 6°. Another stable raster pattern with double non-resonant scanning shown in Fig. 8(c) was generated with Mirror I scanning vertically at 30 Hz and Mirror II scanning horizontally at 5 Hz.

These results have demonstrated the first version of such miniature two-mirror forward-view scanners, but there are still some limitations in this device. On one hand, the two scanning mirrors are fully decoupled, which means the actuation of one mirror will have no effect on the other mirror. However, for either mirror on this device, there still exists a small self coupling, that is, there is still a weak coupling between the two axes of each mirror, which can be noticed in the frequency response in Fig. 7. In addition, due to the microfabrication process imperfections and variations, the two vertical mirrors are not perfectly parallel to each other. Thus, the horizontal and vertical scanning directions of the two mirrors will not be exactly orthogonal to each other. This can explain the twisted scanning pattern shown in Fig. 8(c). How to minimize the effect of the decoupling on the single 2D MEMS mirrors and

how to make the vertical mirrors more parallel to each other need further investigation.

V. Conclusion

In this work, a monolithic forward-view 2-axis MEMS scanner based on SiOB has been successfully demonstrated. Compared to our previous work in [19], the two MEMS mirrors of this new MEMS scanner design can both scan in two axes, which expands the total FoV by a factor of 3. In addition, the new design decouples the tip-tilt resonant frequencies, so decoupled raster scan patterns can be generated by actuating the two vertical MEMS mirrors in two different axes with two different frequencies. The fabricated process is also improved so that the undercut of the sidewalls of the stopper is significantly reduced.

Table III compares this work with other 2-mirror scanning modules. Thanks to the intergration of two vertical scanning mirrors on a single small SiOB, the two scanning mirrors can be closely placed and self-aligned without the need of packaging and alignment. The dimensions of the scanner are at least one order of magnitude smaller than those of other 2-mirror scanning modules without sacrificing the FoV, as shown in Table III. With a weight of only 20 mg, this compact forward-view scanner is ideal for MAVs. It also has other potential applications, such as endoscopic optical imaging and Michelson interferometers.

Acknowledgment

The MEMS devices were fabrication in Nanoscale Research Facility at University of Florida.

References

[1] Z. Xuexi, L. Guokun, F. Genping, X. Dongliang, and L. Shiliu, "SLAM algorithm analysis of mobile robot based on lidar," in *Proc. Chin. Control Conf. (CCC)*, Guangzhou, China, Jul. 2019, pp. 4739–4745.

[2] D. Maturana and S. Scherer, "VoxNet: A 3D convolutional neural network for real-time object recognition," in *Proc. IEEE/RSJ Int. Conf. Intell. Robots Syst. (IROS)*, Hamburg, Germany, Sep. 2015, pp. 922–928.

[3] T. Miyasaka, Y. Ohama, and Y. Ninomiya, "Ego-motion estimation and moving object tracking using multi-layer LIDAR," in *Proc. IEEE Intell. Vehicles Symp.*, Xi'an, China, Jun. 2009, pp. 151–156.

[4] A.-I. Garcia-Moreno and J.-J. Gonzalez-Barbosa, "GPS precision time stamping for the HDL-64E lidar sensor and data fusion," in *Proc. IEEE 9th Electron., Robot. Automot. Mech. Conf.*, Cuernavaca, Mexico, Nov. 2012, pp. 48–53.

[5] K. Ito *et al.*, "System design and performance characterization of a MEMS-based laser scanning time-of-flight sensor based on a 256×64-pixel single-photon imager," *IEEE Photon. J.*, vol. 5, no. 2, Apr. 2013, Art. no. 6800114.

[6] Z. Tasneem, D. Wang, H. Xie, and K. Sanjeev, "Directionally controlled time-of-flight ranging for mobile sensing platforms," in *Robotics: Science and Systems XIV*. 2018, pp. 11–21.

[7] H. W. Yoo *et al.*, "MEMS-based lidar for autonomous driving," *e i Elektrotechnik und Informationstechnik*, vol. 135, no. 6, pp. 408–415, Oct. 2018.

[8] R. Moss *et al.*, "Low-cost compact MEMS scanning ladar system for robotic applications," *Proc. SPIE*, Vol. 8379, May 2012, Art. no. 837903.

[9] A. Kasturi, V. Milanovic, B. H. Atwood, and J. Yang, "UAV-borne lidar with MEMS mirror-based scanning capability," *Proc. SPIE*, Vol. 9832, May 2016, Art. no. 98320M.

[10] K. Kimoto, N. Asada, T. Mori, Y. Hara, A. Ohya, and S. Yuta, "Development of small size 3D LIDAR," in *Proc. IEEE Int. Conf. Robot. Autom. (ICRA)*, Hong Kong, May 2014, pp. 4620–4626.

[11] S. B. Fuller, A. Sands, A. Haggerty, M. Karpelson, and R. J. Wood, "Estimating attitude and wind velocity using biomimetic sensors on a microrobotic bee," in *Proc. IEEE Int. Conf. Robot. Autom.*, Karlsruhe, Germany, May 2013, pp. 1374–1380.

[12] D. Wang, S. Strassle Rojas, A. Shuping, Z. Tasneem, S. Koppal, and H. Xie, "An integrated forward-view 2-Axis mems scanner for compact 3D lidar," in *Proc. IEEE 13th Annu. Int. Conf. Nano/Micro Engineered Mol. Syst. (NEMS)*, Singapore, Apr. 2018, pp. 185–188.

[13] C. Duan *et al.*, "An endoscopic forward-viewing OCT imaging probe based on a two-axis scanning mems mirror," in *Proc. IEEE 11th Int. Symp. Biomed. Imag. (ISBI)*, Beijing, China, Apr. 2014, pp. 1397–1400.

[14] D. Wang, C. Watkins, S. Koppal, and H. Xie, "A silicon optical bench with vertically-oriented micromirrors for active beam steering," *Sens. Actuators A, Phys.*, vol. 298, Oct. 2019, Art. no. 111586.

[15] X. T. Nguyen, V. L. Dinh, H.-J. Lee, and H. Kim, "A high-definition LIDAR system based on two-mirror deflection scanners," *IEEE Sensors J.*, vol. 18, no. 2, pp. 559–568, Jan. 2018.

[16] *Magnetic Deflection Unit*. Sercalo. Accessed: Apr. 21, 2020. [Online]. Available: https://www.sercalo.com/products/pdfs/Magnetic-Deflection-Unit.pdf

[17] S. Gu-Stoppel, J. Janes, H. J. Quenzer, U. Hofmann, and W. Benecke, "Two-dimensional scanning using two single-axis low-voltage PZT resonant micromirrors," *Proc. SPIE*, vol. 8977, Mar. 2014, Art. no. 897706.

[18] *MAR1800-MEMS 2D Vector Scanning Mirror Module*. Maradin. Accessed: Apr. 21, 2020. [Online]. Available: http://www.maradin.co.il/wp-content/uploads/2016/03/MAR1800-DataSheet-201603.pdf

[19] D. Wang, S. Strassle, S. Koppal, A. Stainsby, Y. Bai, and H. Xie, "A compact 3D lidar based on an electrothermal two-axis MEMS scanner for small UAV," *Proc. SPIE*, vol. 10636, May 2018, Art. no. 106360G.

[20] K. Jia, S. Pal, and H. Xie, "An electrothermal tip–tilt–piston micromirror based on folded dual S-shaped bimorphs," *J. Microelectromech. Syst.*, vol. 18, no. 5, pp. 1004–1015, Oct. 2009.

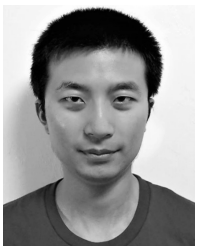

Dingkang Wang received the B.E. degree in mechanical engineering from Jilin University, China, in 2016. He is currently pursuing the Ph.D. degree with the Department of Electrical and Computer Engineering, University of Florida, Gainesville, FL, USA. His research interests include microelectromechanical (MEMS) systems, micro/nano fabrication, and light detection and ranging (LiDAR) systems.

Sanjeev J. Koppal (Senior Member, IEEE) received the B.S. degree from the University of Southern California in 2003, and the master's and Ph.D. degrees from the Robotics Institute, Carnegie Mellon University. After CMU, he was a Post-Doctoral Research Associate with the School of Engineering and Applied Sciences, Harvard University. He is currently an Assistant Professor with the ECE Department, University of Florida. Prior to joining UF, he was a Researcher at the Texas Instruments Imaging Research and Development Lab. His research interests include computer vision, computational photography and optics, novel cameras and sensors, 3D reconstruction, physics-based vision, and active illumination.

Huikai Xie (Fellow, IEEE) received the B.S. degree in electrical and computer engineering from the Beijing Institute of Technology, the M.S. degree in electrical and computer engineering from Tufts University, and the Ph.D. degree in electrical and computer engineering from Carnegie Mellon University. He worked with Tsinghua University, Robert Bosch Company, and US Air Force Research Lab. He joined the University of Florida as an Assistant Professor in 2002, where he is currently a Professor with the Department of Electrical and Computer Engineering. He has published over 300 technical articles and holds more than 30 patents. His research interests include MEMS/NEMS, integrated sensors, microactuators, integrated power passives, CNT-CMOS integration, optical MEMS, LiDAR, micro-spectrometers, optical bioimaging, and endomicroscopy. He is a Fellow of SPIE. He is an Associate Editor of the IEEE Sensors Letters and *Sensors and Actuators A: Physics*.